

# Geometrical dependence of quantum decoherence in circular arenas with side-wires

Yuantao Xie<sup>1</sup>, Clément Le Priol<sup>2</sup> and Jean J Heremans<sup>1</sup>

<sup>1</sup> Department of Physics, Virginia Tech, VA, USA

<sup>2</sup> Department of Physics, Ecole Polytechnique, 91128 Palaiseau, France

E-mail: [heremans@vt.edu](mailto:heremans@vt.edu)

Received 2 June 2016, revised 25 August 2016

Accepted for publication 16 September 2016

Published 18 October 2016



## Abstract

Low-temperature quantum phase coherence lengths were experimentally measured in mesoscopic circular arenas fabricated on InGaAs quantum wells. The arenas are connected to wide sample regions by short side-wires, to investigate the effects of geometry in comparison to intrinsic materials properties on quantum decoherence. Universal conductance fluctuations were used to quantify the phase coherence lengths as a function of temperature and geometry. The experimental data show a dependence of phase coherence lengths on side-wire length and width-to-length ratio, which is accounted for by the competing effects of decoherence by coupling to the classical environment and Nyquist decoherence in ergodic wires. The observed decay of phase coherence lengths with the increasing temperature is consistent with expectations. The work demonstrates that geometrical effects influence the measured mesoscopic quantum decoherence.

Keywords: quantum coherence, mesoscopic physics, quantum wires, quantum transport, universal conductance fluctuations

(Some figures may appear in colour only in the online journal)

## 1. Introduction

Quantum interference phenomena and quantum decoherence in mesoscopic systems have attracted considerable attention. In mesoscopic systems, the quantum phases of carrier states can be randomized by inelastic or quasi-elastic scattering mechanisms such as electron–phonon and electron–electron scattering, and quantum decoherence results [1–4]. Also, the measurement of a quantum system necessitates coupling to the external environment, considered a classical system [5, 6], leading to environmental coupling decoherence [5–8]. At low temperature  $T$ , the inelastic or quasi-elastic scattering mechanisms are mitigated [5], and sufficiently long quantum phase coherence lengths  $L_\phi$  are obtained to study electronic transport phenomena relying on quantum interference [9, 10]. Quantum decoherence has been studied in quantum dots [11–13], quantum wires [14–18], and quantum rings or ring networks [3, 9, 10, 19], among other geometries.

In this work, mesoscopic circular arenas connected to short side-wires were fabricated on an n-type InGaAs quantum well (QW) in an InGaAs/InAlAs heterostructure, and the quantum decoherence was measured and analyzed in these composite device structures. In the arena-wire samples used here, the dependence of the measured  $L_\phi$  on the geometry of the wires shows that the device geometry plays a role in measured decoherence, by modulating both the importance of the environmental coupling decoherence and of decoherence by quasi-elastic electron–electron Nyquist scattering in low-dimensional systems [19–23]. Previous investigations focusing on quantum decoherence in composite or networked device structures include studies on coupled quantum dots or dot arrays [7, 24–26], as well as experimental and theoretical studies on quantum rings or ring arrays [19–21, 27–29]. The present work demonstrates the general importance of geometry in studying and using quantum-coherence phenomena. Knowledge of the effective quantum coherence lengths is

2 nm undoped InP
17 nm undoped $\text{In}_{0.52}\text{Al}_{0.48}\text{As}$
10 nm undoped $\text{In}_{0.53}\text{Ga}_{0.47}\text{As}$ (QW)
7 nm undoped $\text{In}_{0.52}\text{Al}_{0.48}\text{As}$
6 nm $\text{In}_{0.52}\text{Al}_{0.48}\text{As}$ , Si doped $4 \times 10^{18} \text{ cm}^{-3}$
500 nm undoped $\text{In}_{0.52}\text{Al}_{0.48}\text{As}$ buffer
SI InP (001) substrate

**Figure 1.** Layer sequence of the bottom-doped InGaAs/InAlAs heterostructure, with the  $\text{In}_{0.53}\text{Ga}_{0.47}\text{As}$  quantum well (red) located 19 nm below the surface.

important, among other areas, in the characterization of new quantum states of matter, particularly when the quantum states are realized in mesoscopic systems or if the states are expected to exhibit characteristic quantum-coherent transport phenomena only over length scales comparable to their effective quantum coherence lengths.

The length  $L_\phi$  is used as a measure of quantum coherence and is, in this work, measured as function of sample geometry and  $T$ , by universal conductance fluctuations (UCFs), reproducible and aperiodic conductance variations originating in quantum interference in mesoscopic systems [1, 4, 22, 30, 31]. Quantum coherence effects are discernible in the correlation function characterizing UCFs, providing a precise way of extracting values for  $L_\phi$ . Weak-antilocalization (WAL) is also present in the samples [17, 18, 32–34], yet is masked by a strong UCF signal, and UCFs are hence preferred in the present work for obtaining  $L_\phi$ .

## 2. Experiments and analysis

The mesoscopic geometries are fabricated on the InGaAs/InAlAs heterostructure by electron-beam lithography and wet etching. The heterostructure schematically depicted in figure 1 was grown by molecular-beam epitaxy on semi-insulating InP (001) substrate and consists of, from bottom to top, a 500 nm  $\text{In}_{0.52}\text{Al}_{0.48}\text{As}$  buffer, a 6 nm  $\text{In}_{0.52}\text{Al}_{0.48}\text{As}$  n-doping layer, a 7 nm  $\text{In}_{0.52}\text{Al}_{0.48}\text{As}$  spacer, the 10 nm wide  $\text{In}_{0.53}\text{Ga}_{0.47}\text{As}$  electron QW, a 17 nm  $\text{In}_{0.52}\text{Al}_{0.48}\text{As}$  spacer, and a 2 nm undoped InP cap layer. In this lattice-matched structure, the  $\text{In}_{0.52}\text{Al}_{0.48}\text{As}$  doping layer is thus situated below the  $\text{In}_{0.53}\text{Ga}_{0.47}\text{As}$  QW, which leads to an asymmetric QW confinement potential for the two-dimensional electron system (2DES) and hence a substantial spin-orbit interaction, but depresses the electron mobility  $\mu$  in the 2DES, compared with other  $\text{In}_{0.53}\text{Ga}_{0.47}\text{As}/\text{In}_{0.52}\text{Al}_{0.48}\text{As}$  heterostructures [35, 36]. The 2DES areal carrier density  $N_s = 2.02 \times 10^{16} \text{ m}^{-2}$  and  $\mu = 1.49 \text{ m}^2 (\text{Vs})^{-1}$ , evaluated from van der Pauw measurements at  $T = 0.40 \text{ K}$ . Hall effect and Shubnikov-de Haas oscillations yield consistent results for  $N_s$ , and transport parameters do not vary significantly in the range of  $T$  of our measurement, from 0.40 K to 5.0 K. Calculated transport parameters, such as the elastic scattering time  $\tau_e = 0.97 \text{ ps}$ , the mean-free path  $\lambda_e = 0.77 \mu\text{m}$  ( $T = 0.40 \text{ K}$ ) and the electron diffusion

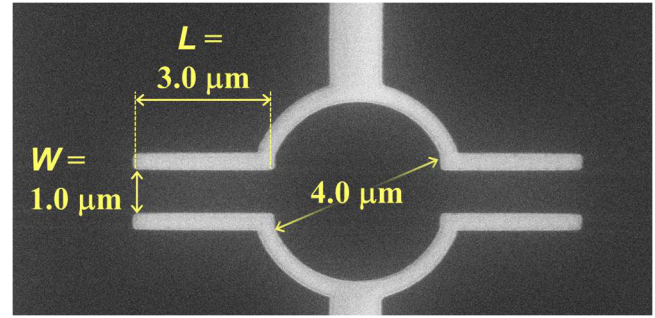


**Figure 2.** Scanning electron micrograph of a typical circular arena with side-wires. The lighter areas depict wet-etched trenches forming insulating barriers for the quantum well electrons, and delineating the devices. The central circular arenas in all samples have diameter  $4.0 \mu\text{m}$ , while the width  $W$  and length  $L$  of the connecting side-wires vary (here  $W = 1.0 \mu\text{m}$ ,  $L = 3.0 \mu\text{m}$ ).

**Table 1.** Widths  $W$  and lengths  $L$  of the connecting side-wires of the mesoscopic geometries A, B, C, D, referring to figure 2.

Sample ( $\mu\text{m}$ )	A	B	C	D
$W$	1.4	1.0	1.0	0.6
$L$	1.0	1.0	3.0	1.0
$L_\phi$	2.17	2.06	1.92	1.82

Note: The measured quantum phase coherence lengths  $L_\phi$  ( $T = 0.40 \text{ K}$ ) are obtained by the method illustrated in figure 5 (cfr. text).

coefficient  $D = 0.30 \text{ m}^2 \text{ s}^{-1}$ , are evaluated accounting for nonparabolicity in the InGaAs conduction band, with a ratio of  $\Gamma$ -point effective mass  $m$  to free-electron mass of 0.0353 and a low  $T$  band gap of 813 meV. The calculated Fermi wavelength  $\lambda_F = 17.6 \text{ nm}$ , much smaller than the mesoscopic dimensions of the samples. Figure 2 contains a micrograph of a typical arena-wire geometry used in this work, with the characteristic dimensions indicated. The diameter of arenas is fixed at  $4.0 \mu\text{m}$ , while the widths  $W$  and lengths  $L$  of the connecting side-wires vary as enumerated in table 1, where labels A to D denote the measured samples. Measurements occurred in a  $^3\text{He}$  cryostat by standard four-contact lock-in techniques under a constant low-frequency ac current  $I = 20 \text{ nA}$ , sufficiently low to avoid affecting the electron  $T$ .

As example, figure 3 shows data for conductance  $G$  versus magnetic field  $B$  (magnetoconductance) obtained on arena D, parametrized in  $T$ . UCFs are clearly visible, diminishing in amplitude with increasing  $T$ , as expected. Around  $B \sim 0$  a negative magnetoconductance due to WAL is also present [17, 18, 32–34], but is not used for analysis in the present work. We extracted  $L_\phi$  by fitting a correlation function to the UCF data, with the correlation function defined as [11, 37]

$$\overline{\delta G(B)\delta G(B + \Delta B)} = \langle [G(B) - \langle G(B) \rangle][G(B + \Delta B) - \langle G(B) \rangle] \rangle \quad (1)$$

in which the angled brackets denote an average over a range of  $B$ . We obtain [38],

$$\overline{\delta G(B)\delta G(B + \Delta B)} = f \left( \frac{\Delta B}{2B_\phi} \right) \quad (2)$$

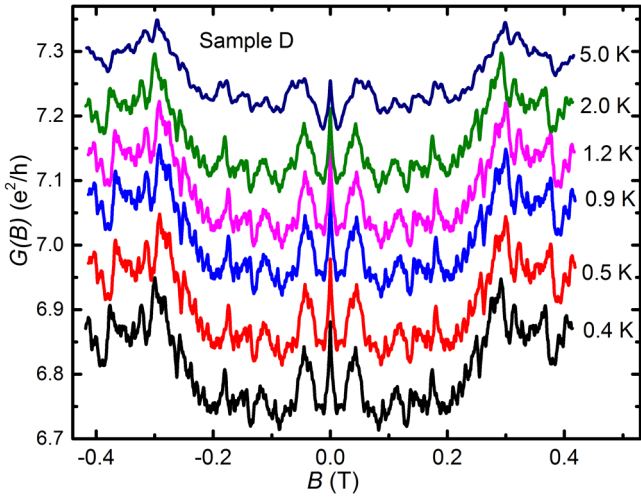


**Figure 3.** Magnetoconductance of sample D measured at different  $T$ , from 0.40 K to 5.0 K (data offset for clarity). Clear UCFs ride on a magnetoconductance background. At  $T < 1.0$  K, the amplitude of the UCFs depends weakly on  $T$ , consistent with a saturation of  $L_\phi$ , while for  $T > 1.0$  K the amplitude decreases notably with increasing  $T$ . Around  $B \sim 0$ , a WAL negative magnetoconductance signal is present with amplitude comparable to the UCFs.

under the condition  $B \gg B_\phi$ , where the characteristic field  $B_\phi$  is in the diffusive approximation defined as [39]

$$B_\phi = \hbar/(4eD\tau_\phi) \quad (3)$$

where  $\tau_\phi$  denotes the quantum phase coherence time, and  $L_\phi = \sqrt{D\tau_\phi}$ .  $B_\phi$  characterizes the field under which one flux quantum  $h/e$  threads the area  $8\pi L_\phi^2$ . In equation (2),  $f(x)$  is defined as

$$f(x) = \overline{\delta G^2(B)} \frac{1}{x} \Psi' \left( \frac{1}{2} + \frac{1}{x} \right) \quad (4)$$

where  $\Psi(x)$  is the digamma function. Here  $\delta G^2(B)$  denotes  $\overline{\delta G(B)\delta G(B + \Delta B)}$  evaluated at  $\Delta B = 0$  (equation (2)) [38], and is calculated as a  $B$ -independent average over  $B$ .

Figure 4 depicts a correlation function calculated according to equation (1) for arena D, at  $T = 0.40$  K. A high-pass filter was first applied to the magnetoconductance data (example in figure 3) to remove a slowly varying background due to classical magnetoconductance. The correlation function was calculated by averaging over  $B$  for  $0.04 \text{ T} \leq B \leq \sim 0.36 \text{ T}$  thereby avoiding the WAL signal at low  $B$ . Further, estimating preliminarily  $L_\phi \approx 1 \mu\text{m}$ , we find  $B_\phi \approx 0.16 \text{ mT} \ll 0.04 \text{ T}$  such that  $B \gg B_\phi$  is also satisfied. Equation (2) was then used to fit the correlation function, as depicted in figure 4. The decay of the correlation function with increasing  $\Delta B$  is expected at low  $\Delta B$ , reflecting the increasingly uncorrelated UCFs as  $\Delta B$  increases, and figure 4 indeed shows that equation (2) provides a good fit at low  $\Delta B$ . At higher  $\Delta B$  the fit does not include the quasi-periodic oscillation visible in figure 4, also frequently observed in other work [30, 37, 40]. The quasi-periodic oscillation originates in a fluctuation in the density of states [31, 40] related to pointer states [6, 31]. Under varying  $B$  the Fermi energy migrates through the energy levels of pointer states, which leads to oscillations in magnetoconductance, visible in

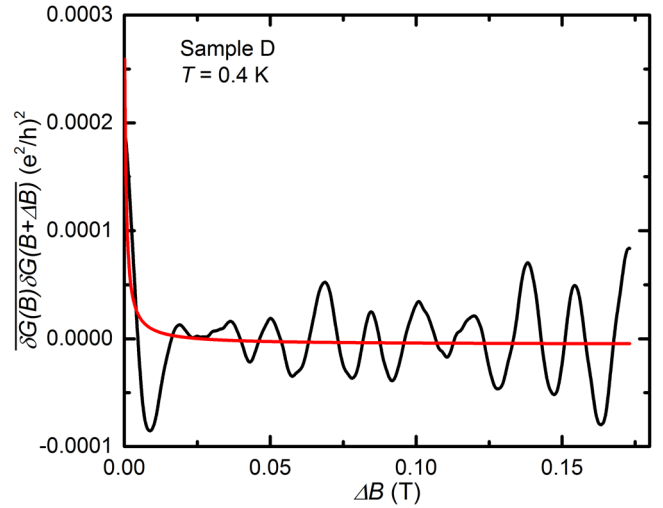


**Figure 4.** Correlation function for sample D, based on experimental data at  $T = 0.40$  K. The black curve represents the correlation function calculated from experimental data using equation (1). The red curve represents the correlation function fitted according to equation (2), with  $L_\phi = \sqrt{D\tau_\phi}$  as fitting parameter.

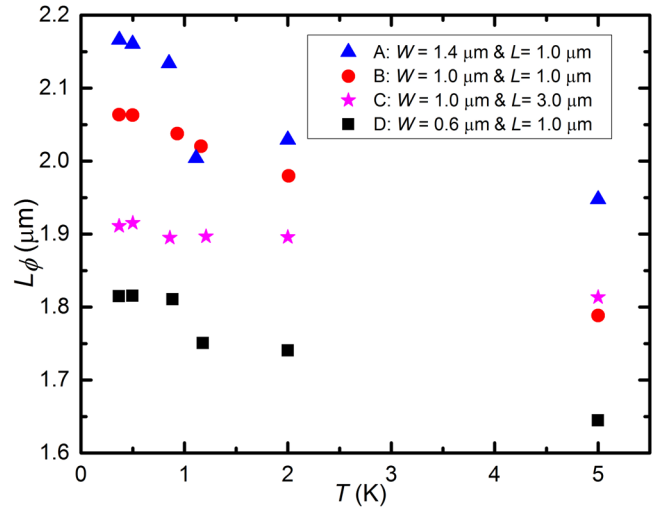


**Figure 5.**  $L_\phi$  versus  $T$  extracted from the UCF data for samples A, B, C, D by fitting equation (2). As expected, for  $T < 1.0$  K,  $L_\phi$  shows saturation in  $T$ , while for  $T > 1.0$  K,  $L_\phi$  decreases with increasing  $T$ . Concerning geometrical dependence,  $L_\phi$  decreases according to the sample series A  $\rightarrow$  B  $\rightarrow$  C  $\rightarrow$  D.

the correlation function in figure 4. For our samples, the correlation functions result from a superposition of a decaying contribution from UCFs and a quasi-periodic contribution from pointer states. Due to the obvious difference between the two contributions, extraction of  $B_\phi$  by fitting with equation (2) is possible.

Fitting equation (2) with  $B_\phi$  as fitting parameter for samples A to D and for all discrete measurement  $T$ , yields the values of  $L_\phi$  depicted in figure 5. It is apparent that  $L_\phi$  decreases according to the series of samples A  $\rightarrow$  B  $\rightarrow$  C  $\rightarrow$  D. To validate the results and conclusions, another approach was used as well to obtain  $B_\phi$ , based on the half-width at half-maximum of the correlation function [11, 38]:

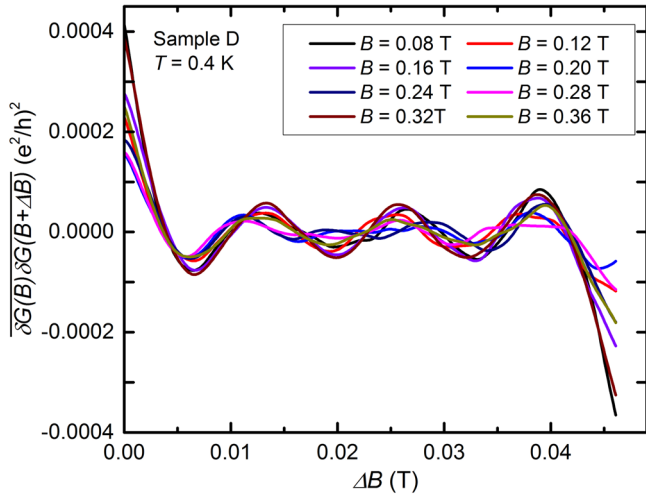


**Figure 6.** Correlation functions for sample D, based on experimental data at  $T = 0.40$  K and calculated using equation (1). The data was sectioned into spans of  $B$  of range  $0.08$  T, and the correlation function calculated over this range around the center  $B$  as indicated. A bandpass filter was applied to mitigate oscillations as discussed in the text.

$$\overline{\delta G(B)\delta G(B + 12.4B_\phi)} = \overline{\delta G^2(B)}/2 \quad (5)$$

Under this definition,  $B_\phi$  is the half-width of correlation function. The analysis using equation (5) also allows us to ascertain the corrections due to ballistic transport over the scale of the cyclotron radius,  $\sim 1.3 \mu\text{m}$  in the range of  $B$  used for the analysis, can be neglected [1, 41]. The ballistic corrections may influence results if the device size ( $\sim 4 \mu\text{m}$ ), the cyclotron radius, and  $\lambda_e = 0.77 \mu\text{m}$  are comparable. The data was divided into equal sections of  $B$  of length  $0.08$  T, and the correlation function was calculated over this range of  $0.08$  T around a center  $B$ . To mitigate the oscillations discussed above, a bandpass filter was applied to the calculated correlation functions. In figure 6, the filtered correlation functions for the different sections of  $B$  are shown, labeled by their center  $B$ . From the calculated correlation functions as function of center  $B$  and of  $T$ , the  $B_\phi$  (equation (5)) and  $L_\phi$  were deduced. The dependence on center  $B$  indicated that the corrections due to ballistic transport can indeed be neglected. Values for  $L_\phi$  for samples A–D were obtained as averages over center  $B$  and over  $T$  to provide a comparison with the values in figure 5. The analysis using equation (5) and subsequent averaging yields for sample A,  $L_\phi = 1.26 \mu\text{m}$ ; for sample B,  $L_\phi = 1.15 \mu\text{m}$ ; for sample C,  $L_\phi = 1.14 \mu\text{m}$ ; for sample D,  $L_\phi = 1.09 \mu\text{m}$ . The values reproduce the observation that  $L_\phi$  decreases according to the series of samples  $A \rightarrow B \rightarrow C \rightarrow D$ . The relative values of  $L_\phi$  are also approximately maintained, as the values according to equation (5) are a fixed factor  $\sim 1.6$  lower than the averages over  $T$  of the values found in figure 5. A more accurate correspondence should not be expected, since the sectioning in ranges of  $B$ , the bandpass filtering, and the averaging over  $B$  and  $T$  amount to data treatments that will affect absolute values of  $L_\phi$ . While the analysis using equation (5) is hence not preferred for the most accurate values, it does extract from the UCF data the same observation as figure 5 about the decrease in  $L_\phi$  according to the series  $A \rightarrow B \rightarrow C \rightarrow D$ .

### 3. Discussion of results

The values of  $L_\phi$  contained in figure 5, with the values at  $T = 0.40$  K repeated in table 1, show that  $L_\phi$  is similar or only somewhat below the relevant geometrical length scales of the arena diameter,  $L$  and  $W$ . Therefore quantum coherence phenomena and in particular UCFs will not average out and will be prominent, as observed and as typical for mesoscopic systems. Decoherence effects impacting quantum coherence in the system composed of arena and side-wires, are indeed visible and can be analyzed as described below. It is to be noted that the system is not in the fully diffusive regime ( $L_\phi \ll$  system size), but closer to the ergodic regime [19–21, 28, 38].

From figure 5 the dependence on  $T$  of  $L_\phi$  is apparent. In agreement with theoretical and experimental work [1, 2, 16, 17, 19–22],  $L_\phi$  decreases with increasing  $T$ , and at the lower  $T < 1$  K,  $L_\phi$  tends to saturate (the saturation has been extensively discussed in the literature [2, 13, 17, 22, 23, 42]). The saturated values of  $L_\phi$  obey the same sample dependence as observed over  $0.40 \text{ K} < T < 5.0 \text{ K}$  (namely  $L_\phi$  decreasing from  $A \rightarrow B \rightarrow C \rightarrow D$ ), and are listed in table 1. For  $T > 1$  K, the data in figure 5 yields  $L_\phi \sim T^{-p/2}$  with  $p/2 \approx 0.06 \dots 0.08$ , leading to a decoherence rate  $\tau_\phi^{-1} \sim T^p$  with  $p \approx 0.12 \dots 0.16$ . At low  $T$ , the dependence on  $T$  of  $\tau_\phi^{-1}$  can originate in electron–electron scattering with large energy transfer [1, 2, 4, 16, 20, 22] with decoherence rate  $\tau_{ee}^{-1} \sim T^2$  in both 1D (wires) and 2D (arenas), or can originate in electron–phonon scattering with  $\tau_{ep}^{-1} \sim T^q$  with  $q$  experimentally determined as  $2 \dots 4$  [2, 22], or can originate in thermal broadening of energy levels beyond the Thouless energy, leading to averaging over incoherent independent channels, with decoherence rate  $\tau_T^{-1} \sim T^{1/2}$  [10]. Yet often limiting  $\tau_\phi$  at low  $T$  is quasi-elastic electron–electron Nyquist scattering [19, 21–23, 27], with a decoherence rate  $\tau_N^{-1} \sim T^n$ , where  $n$  depends on the geometry. Nyquist scattering results from dephasing of the state of a given electron by the fluctuating electromagnetic environment created by the other electrons. The geometry and how the geometry is sampled by the electron trajectories influence the effects of the potential fluctuations, resulting in a dependence on geometry of Nyquist scattering and of its dependence on  $T$  in mesoscopic devices [19, 21, 27]. In a long wire of width  $W$  in the diffusive regime ( $L \gg L_\phi$ ), the Nyquist length  $L_N = \sqrt{D\tau_N}$  is expressed as [3, 19, 21]  $L_N = \sqrt{2(mWD^2/(\pi k_B T))}^{1/3}$ , where  $k_B$  denotes the Boltzmann constant. Hence in this diffusive 1D regime  $\tau_N^{-1} \sim T^{2/3}$  (while  $\tau_N^{-1} \sim T$  in 2D). Yet, in a shorter 1D wire, diffusive trajectories are limited to the wire length  $L$ , and the trajectories can explore the whole length of the wire. In this ergodic regime, the Thouless time  $\tau_D = L^2/D < \tau_\phi$ , and the relevant modified Nyquist decoherence length  $L_C$  is given by [19–21, 28]  $L_C = \sqrt{D\tau_C} = \sqrt{L_N^3/L} = 2^{3/4}D\sqrt{mW/(\pi k_B TL)}$ . The dependence of  $L_C$  on geometry via  $\sqrt{W/L}$  is explicit, as is the dependence  $\tau_C^{-1} \sim T$ . The dependence on  $T$  of  $\tau_\phi^{-1}$  can be approximated as resulting from the sum of the above decoherence rates, thus leading to the expectation  $\frac{1}{2} \leq p \leq 4$ . The

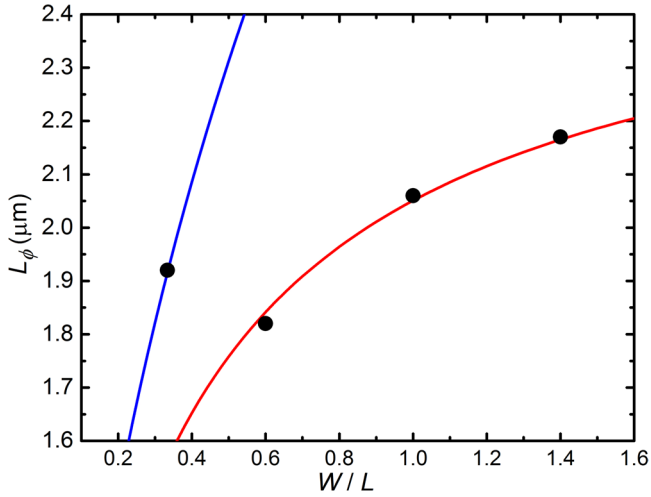


**Figure 7.**  $L_\phi$  versus side-wire  $W/L$ , extracted from the UCF data for samples A, B, C, D at  $T = 0.40$  K, represented as black solid circles. The red and blue solid lines represent the fit to equation (6), plotted for  $L = 1.0 \mu\text{m}$  and  $L = 3.0 \mu\text{m}$ , *resp.*

observed  $p$  denotes a substantially weaker dependence on  $T$ , indicating that  $\tau_\phi$  is in the regime of  $T$  of the experiments subject to limits imposed by decoherence mechanisms insensitive to  $T$ . Such a mechanism can be found in quantum decoherence due to environmental coupling.

In figure 7,  $L_\phi$  (at  $T = 0.40$  K, in the saturation regime) is plotted versus  $W/L$  of the connecting side-wires. The datapoint at  $W/L = 0.33$  corresponds to  $L = 3.0 \mu\text{m}$  and  $W = 1.0 \mu\text{m}$ , while the datapoints with  $W/L \geq 0.60$  all correspond to fixed  $L = 1.0 \mu\text{m}$  and variable  $W = 0.6 \mu\text{m}$ ,  $1.0 \mu\text{m}$  and  $1.4 \mu\text{m}$ . Two geometrical parameters appear to influence  $L_\phi$ , namely  $W/L$  and  $L$ . Table 1 and figure 7 show that  $L_\phi$  increases with increasing  $W/L$  for  $L = 1.0 \mu\text{m}$ , yet also increases at longer  $L = 3.0 \mu\text{m}$  ( $W/L = 0.33$ ). The effect of increasing  $L$  can be captured by the influence of environmental coupling decoherence, expressing the total decoherence rate as  $\tau_\phi^{-1} = \tau_{\phi 0}^{-1} + \tau_d^{-1}$ . Here the second term denotes an escape rate with  $\tau_d$  a dwell time, and is identified with quantum decoherence due to environmental coupling [5, 8]. The first term then equals the decoherence rate for an isolated system, with  $\tau_d \rightarrow \infty$ . A longer  $\tau_d$  corresponds to weaker environmental coupling, longer  $\tau_\phi$  and longer  $L_\phi$ . For a diffusive wire with  $L > \lambda_e$ , as is the case for  $L = 3.0 \mu\text{m}$ , we can estimate the probability for an electron emerging from the arena into the wire to be reflected back into the arena as  $P = 1 - \lambda_e/L$ . Then  $\tau_d \propto P/(1 - P) = (L/\lambda_e) - 1$ , expressing that a longer side-wire will lead to reduced escape rate and longer  $\tau_\phi$ . We attribute the rise in  $L_\phi$  at longer  $L = 3.0 \mu\text{m}$  ( $W/L = 0.33$ ) to this dependence on  $L$  of the environmental coupling decoherence rate  $\tau_d^{-1}$ . Figure 7 shows that  $L_\phi$  increases with  $W$  at constant  $L$ . This trend is initially surprising given the expectation that in lateral quantum dots [5, 8], the wider the aperture connecting the quantum dots to the environment the shorter  $L_\phi$ , since a wider aperture corresponds to shorter  $\tau_d$ . Yet for a

short wire,  $L_C \propto \sqrt{W/L}$  as found above. We surmise that the approximate dependence  $L_\phi \propto \sqrt{W/L}$  observed in figure 7 for  $W/L \geq 0.60$  arises from  $L_C$  limiting  $L_\phi$  in the side-wires, since we measure the effective  $L_\phi$  averaged over all decoherence phenomena occurring over the composite device. In this view, we surmise that  $\tau_N^{-1}$  has a determining role in  $\tau_\phi^{-1}$ . We note that ascribing the observed dependence of  $L_\phi$  on geometry to environmental coupling decoherence and Nyquist decoherence is a phenomenological description fitting this particular device configuration. The fact that the relevant length scales  $L_\phi$ ,  $\lambda_e$ , the arena diameter,  $L$  and  $W$  are similar and hence do not lie at limits assumed by theoretical arguments, introduces uncertainties in a decisive quantitative model for the decoherence phenomena in this compound system. Within the phenomenological description, converting from decoherence rates to lengths, we express the low  $T$  values of  $L_\phi$  with

$$\frac{1}{L_\phi^2} = \frac{1}{L_\alpha^2((L/\lambda_e) - 1)} + \frac{1}{L_\beta^2(W/L)} \quad (6)$$

where  $L_\alpha$  and  $L_\beta$  are fitting parameters.

A fit of equation (6) to the data in table 1 is depicted alongside the data in figure 7, for fitting values  $L_\alpha = 4.69 \mu\text{m}$  and  $L_\beta = 3.42 \mu\text{m}$  (fitting curves are parametrized in  $L$ ). The phenomenological expression equation (6) captures the measured  $L_\phi$  well and in particular reproduces the observed  $\sqrt{W/L}$  dependence. Experimentally in the present work it is hence found that  $L_\phi$  in the given arena-wire geometries can be understood from an interplay between environmental coupling decoherence and Nyquist decoherence in the ergodic short wires.

#### 4. Conclusions

In conclusion, quantum decoherence was investigated in mesoscopic geometries composed of circular arenas coupled to short side-wires, by universal conductance fluctuations in quantum transport at low  $T$ . The mesoscopic geometries were fabricated on InGaAs quantum wells. A dependence of the quantum phase coherence length on side-wire length and side-wire width-to-length ratio was experimentally observed. Phenomenologically, an expression accounting for environmental coupling decoherence and Nyquist decoherence in the side-wires accounts for the observations. The present work underlines the importance of device geometry in using and quantifying quantum-coherence phenomena, a realization of foundational interest as well as of increasing relevance for quantum technologies.

#### Acknowledgments

The work was supported by the U.S. Department of Energy, Office of Basic Energy Sciences, Division of Materials Sciences and Engineering under award DOE DE-FG02-08ER46532.

## References

- [1] Hackens B, Delfosse F, Faniel S, Gustin C, Boutry H, Wallart X, Bollaert S, Cappy A and Bayot V 2002 *Phys. Rev. B* **66** 241305
- [2] Lin J J and Bird J P 2002 *J. Phys.: Condens. Matter* **14** R501
- [3] Ferrier M, Angers L, Rowe A C H, Guéron S, Bouchiat H, Texier C, Montambaux G and Mailly D 2004 *Phys. Rev. Lett.* **93** 246804
- [4] Huibers A G, Switkes M, Marcus C M, Campman K and Gossard A C 1998 *Phys. Rev. Lett.* **81** 200
- [5] Bird J P, Micolich A P, Linke H, Ferry D K, Akis R, Ochiai Y, Aoyagi Y and Sugano T 1988 *J. Phys.: Condens. Matter* **10** L55
- [6] Ferry D K, Burke A M, Akis R, Brunner R, Day T E, Meisels R, Kuchar F, Bird J P and Bennett B R 2011 *Semicond. Sci. Technol.* **26** 043001
- [7] Elhassan M, Bird J P, Akis R, Ferry D K, Ida T and Ishibashi K 2005 *J. Phys.: Condens. Matter* **17** L351
- [8] Bird J P, Micolich A P, Ferry D K, Akis R, Ochiai Y, Aoyagi Y and Sugano T 1998 *Solid-State Electron.* **42** 1281
- [9] Ren S L, Heremans J J, Vijayaragunathan S, Mishima T D and Santos M B 2015 *J. Phys.: Condens. Matter* **27** 185801
- [10] Ren S L, Heremans J J, Gaspé C K, Vijayaragunathan S, Mishima T D and Santos M B 2013 *J. Phys.: Condens. Matter* **25** 435301
- [11] Bird J P, Ishibashi K, Ferry D K, Ochiai Y, Aoyagi Y and Sugano T 1995 *Phys. Rev. B* **51** 18037
- [12] Marcus C M, Westervelt R M, Hopkins P F and Gossard A C 1993 *Phys. Rev. B* **48** 2460
- [13] Pivin D P, Andresen A, Bird J P and Ferry D K 1999 *Phys. Rev. Lett.* **82** 4687
- [14] Doucot B and Rammal R 1986 *J. Phys.* **47** 973
- [15] Chandrasekhar V, Santhanam P and Prober D E 1991 *Phys. Rev. B* **44** 11203
- [16] Niimi Y, Baines Y, Capron T, Mailly D, Lo F Y, Wieck A D, Meunier T, Saminadayar L and Bäuerle C 2010 *Phys. Rev. B* **81** 245306
- [17] Kallaher R L, Heremans J J, Goel N, Chung S J and Santos M B 2010 *Phys. Rev. B* **81** 035335
- [18] Kallaher R L, Heremans J J, Roy W V and Borghs G 2013 *Phys. Rev. B* **88** 205407
- [19] Ferrier M, Rowe A C H, Guéron S, Bouchiat H, Texier C and Montambaux G 2008 *Phys. Rev. Lett.* **100** 146802
- [20] Capron T, Texier C, Montambaux G, Mailly D, Wieck A D and Saminadayar L 2013 *Phys. Rev. B* **87** 041307
- [21] Texier C, Delplace P and Montambaux G 2009 *Phys. Rev. B* **80** 205413
- [22] Rudolph M and Heremans J J 2011 *Phys. Rev. B* **83** 205410
- [23] Natelson D, Willett R L, West K W and Pfeiffer L N 2001 *Phys. Rev. Lett.* **86** 1821
- [24] Elhassan M et al 2001 *Phys. Rev. B* **64** 085325
- [25] Aoki N, Oonishi D, Iwase Y, Ochiai Y, Ishibashi K, Aoyagi Y and Bird J P 2002 *Appl. Phys. Lett.* **80** 2970
- [26] Fairbanks M S, Martin T P, Scannell B C, Marlow C A, Linke H and Taylor R P 2010 *Physica E* **42** 1205
- [27] Texier C 2007 *Phys. Rev. B* **76** 153312
- [28] Texier C and Montambaux G 2005 *Phys. Rev. B* **72** 115327
- [29] Ludwig T and Mirlin A D 2004 *Phys. Rev. B* **69** 193306
- [30] Jalabert R A, Baranger H U and Stone A D 1990 *Phys. Rev. Lett.* **65** 2442
- [31] Ferry D K, Akis R A, Pivin D P, Bird J P, Holmberg N, Badrieh F and Vasileska D 1998 *Physica E* **3** 137
- [32] Bergmann G 2010 *Int. J. Mod. Phys. B* **24** 2015
- [33] McPhail S, Yasin C E, Hamilton A R, Simmons M Y, Linfield E H, Pepper M and Ritchie D A 2004 *Phys. Rev. B* **70** 245311
- [34] Deo V, Zhang Y, Soghomonian V and Heremans J J 2015 *Sci. Rep.* **5** 9487
- [35] Matsuoka T, Kobayashi E, Taniguchi K, Hamaguchi C and Sasa S 1990 *Japan. J. Appl. Phys.* **29** 2017
- [36] Diez E, Chen Y P, Avesque S, Hilke M, Peled E, Shahar D, Cerveró J M, Sivco D L and Cho A Y 2006 *Appl. Phys. Lett.* **88** 052107
- [37] Akis R, Ferry D K and Bird J P 1996 *Phys. Rev. B* **54** 17705
- [38] Akkermans E and Montambaux G 2007 *Mesoscopic Physics of Electrons and Photons* (Cambridge: Cambridge University Press)
- [39] Marcus C M, Clarke R M, Chan I H, Duruöz C I and Harris J S 1994 *Semicond. Sci. Technol.* **9** 1897
- [40] Ferry D K, Akis R and Bird J P 2005 *J. Phys.: Condens. Matter* **17** S1017
- [41] Bird J P, Ferry D K, Akis R, Ochiai Y, Ishibashi K, Aoyagi Y and Sugano T 1996 *Europhys. Lett.* **35** 529
- [42] Mohanty P, Jariwala E M Q and Webb R A 1997 *Phys. Rev. Lett.* **78** 3366